Chapter 4

Thermal test results on a module with a small sensor

4.1 Module thermal tests experimental setup

As described in Chapter 2, a module was assembled using the same materials as the fully functional modules. This module was used to carry out a series of thermal tests at the CERN Low Temperature Laboratory in order to understand the thermal behaviour and compare it to the finite element simulations. In this chapter a description of the test setup, methodology of analysis and results are presented. These results are compared to the simulations for re-calibration of the model.

Test stand for heat transfer measurements

The experimental setup, which was initially prepared for heat transfer measurements in microtubes at cryogenic temperatures [27], was slightly modified to carry out the thermal tests on the mechanical module (see Figure 4.1).

Figure 4.1 Experimental setup for heat transfer measurements in microtubes at cryogenic temperatures sitting at the Low Temperature Laboratory at CERN [27].

Argon is circulated in a closed circuit, which is designed for a maximum operating pressure of 25 bar. The circuit, shown in Figure 4.2 consists of a warm part and a cold part: the warm part comprises a compressor unit to drive the fluid, a filtering system, a flowmeter and gas handling components; the cold part is installed in a vacuum chamber (10^{-6} mbar) and is linked to the warm part by an internal heat exchanger. Inside the chamber, the mechanical module is sitting close to the thermal interface and the electrical pre-heater. The thermal interface is attached to the cold finger of a cryocooler, which is the heat sink providing the cooling power. A thermal shield surrounds all the cold components and is heat-sinked to the cold finger to minimize thermal radiation to the module.

The thermal interface consists of a condenser and a reservoir in the upper volume and a sub-cooler heat exchanger in the lower volume. The reservoir is operated under saturation conditions (liquid-vapour equilibrium). The pre-heater is then used to achieve the desired temperature or quality (vapour fraction) of the working fluid at the module inlet. The fluid flow rate is controlled with a by-pass valve in the compressor unit and a metering valve.

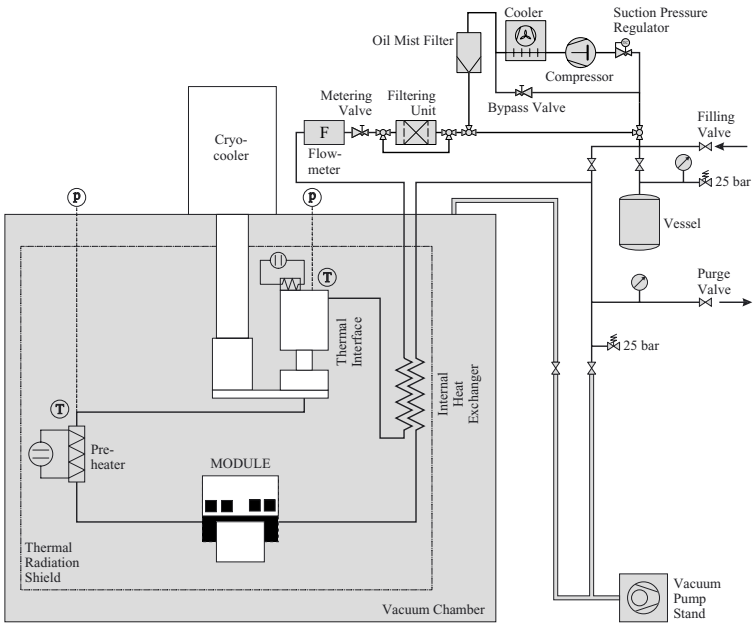

Figure 4.2 Experimental setup for heat transfer and thermal module tests.

Mechanical module

Silicon was used as the basic constructive material for the support plate, pitch adapter and sensor, as well as for the APV25 for the tested dummy module (see Figure 4.3). The hybrid was built on Al_2O_3, and the 0.6 mm OD CuNi capillary pipe was embedded in a carbon fiber composite (CFC) structure, as described in Chapter 2. The dimensions and materials of the different components are listed in Table 4.1.

Table 4.1 Dimensions and materials of the tested mechanical module.

Element	Dimensions (mm^3)	Material
Sensor	30 x 30 x 0.3	Silicon
Support Plate	63 x 47 x 0.3	Silicon
Pitch Adapter	9 x 47 x 0.3	Silicon
Hybrid	30 x 47 x 0.3	Alumina
Pipe	0.6 OD / 0.5 ID	CuNi
Spacer	9 x 47 x 0.3	Carbon Fiber Composite
Glue Layers	100 to 300 μm thickness	Araldite® 2011

The module was instrumented with 8 4-lead temperature sensors located at the thermal interface and distributed on the module. All of them are heat-sinked to the cryocooler. The position of the eight Pt-100 thermometers is shown in Table 4.2.

Thermometer TS8, located at the back of the support plate, was moved to the module outlet to carry out a series of pressure drop calibration runs (see Section 4.3).

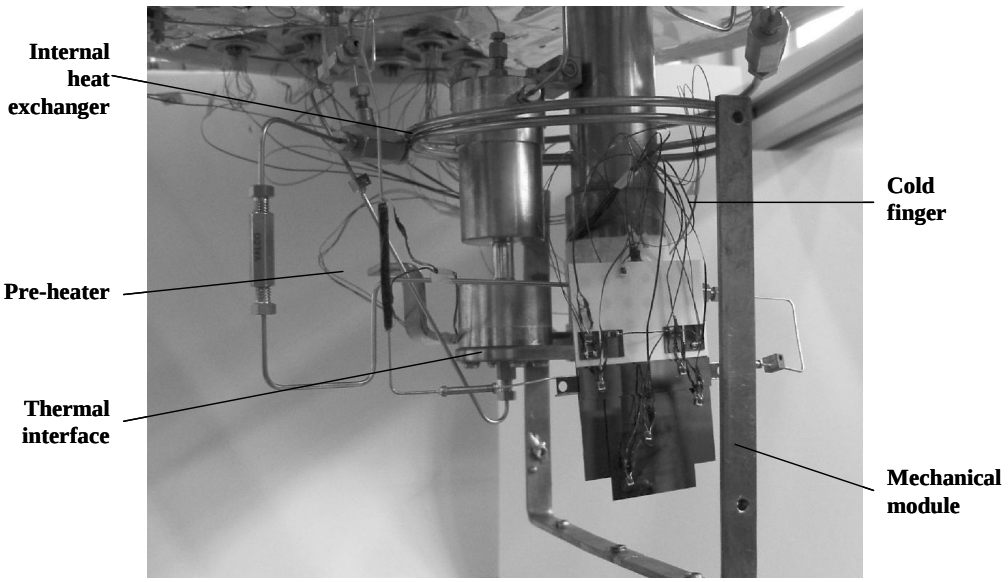

Figure 4.3 The instrumented mechanical module sitting at the test stand.

One 70 Ω MINCO film heater was glued at the back of the support plate in order to simulate thermal radiation. Four 30 Ω surface mounted ceramic heaters are glued on the APVs to reproduce the 2.31 mW/channel heat load of the chips.

A pressure sensor - operated at room temperature and connected to the cold circuit through capillary tubes - was located at the thermal interface. All the instruments are read through GPIB interface on a PC with LabView.

Table 4.2 Position of the Pt-100 thermometers on the mechanical module.

Sensor	Position on the module	
TS1	Pitch adapter	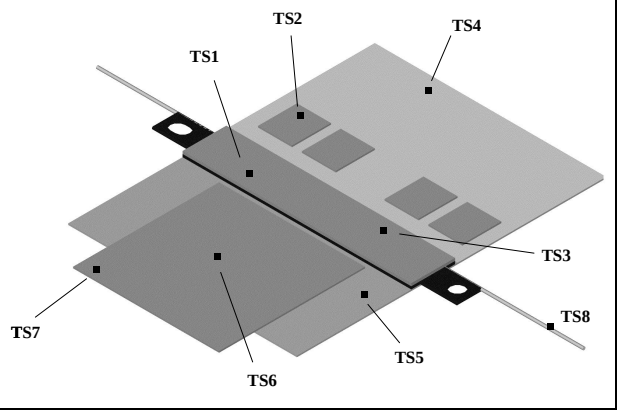
TS2	APV-25	
TS3	Pitchadapter (on top of cooling pipe)	
TS4	Hybrid	
TS5	Support Plate	
TS6	Center of the sensor	
TS7	Extreme of the sensor	
TS8	Back support plate / Outlet module pipe	
CSB	Thermal Interface	

4.2 Enthalpy balance in two-phase flow

The fluid coming from the thermal interface enters the pre-heater in the sub-cooled liquid phase, which allows to determine its thermodynamical state from temperature (CSB) and pressure measurements. The single-phase liquid temperature or two-phase fluid quality at the module inlet/outlet is controlled by the pre-heater power and the thermal load on the electronics and radiation heaters.

The enthalpy at the inlet of the module (h_{inlet}) is calculated making a simple energy balance, from the sub-cooled liquid enthalpy and the power applied to the pre-heater

$$h_{\mathrm{inlet}} = h_{\mathrm{SC}}(p, CSB) + \frac{P_{\mathrm{PH}}}{\dot{m}} , \tag{4.1}$$

where h_{SC} is the enthalpy of the sub-cooled liquid before the pre-heater, P_{PH} the pre-heater power and $\dot{m}$ the mass flow. In an analog way, the enthalpy at the outlet of the module (h_{outlet}) can be calculated by:

$$h_{\mathrm{outlet}} = h_{\mathrm{SC}}(p, CSB) + \frac{P_{\mathrm{PH}} + P_{\mathrm{RAD}} + P_{\mathrm{APV}}}{\dot{m}} , \tag{4.2}$$

where P_{RAD}, P_{APV} are the power applied to the radiation heater and electronics, respectively.

The fraction of the mass flow rate which is vapour in two-phase flow can be calculated by:

$$x = \frac{h - h'}{h'' - h'} , \tag{4.3}$$

where h stands for the enthalpy of a point in the two-phase area with quality factor x, h' is the enthalpy of the saturated liquid and h'' is the enthalpy of the saturated vapour.

The GASPAK[1] integrated package of thermodynamic equations for properties of fluids was used for the evaluation of the fluid properties.

4.3 Pressure drop measurement

During a first set of runs, the temperature at the module outlet was not measured. Therefore, the saturation temperature of the fluid had to be calculated using the pressure measurement at the thermal interface. To obtain the pressure at the module outlet, this measurement had to be corrected with the pressure drop along the pre-heater and the module sections (see Figure 4.2). These sections have inner diameters of 250 μm and 500 μm respectively.

Several runs were dedicated to study the pressure drop at different mass flow rates and quality factors. The homogeneous two-phase flow pressure drop model [25] was compared to the experimental data, and proved to be in good agreement. Consequently, the saturation temperature corrections for the experimental data were done using this model[2].

Homogenous pressure drop model

In single-phase flow, the total pressure gradient along a channel can be expressed as the sum of three components, which arise from distinct physical effects:

$$\begin{array}{lllll} \text{total} & \text{frictional} & \text{gravitational} & \text{accelerational} & \\ \text{pressure} = & \text{pressure} + & \text{pressure} + & \text{pressure} & \\ \text{gradient} & \text{gradient} & \text{gradient} & \text{gradient} & \end{array} \tag{4.4}$$

Single-phase pressure drop (Δp) is generally expressed in the form [27]:

$$\Delta p = \xi \cdot \frac{L}{d} \cdot \frac{\rho \cdot \omega^2}{2}, \tag{4.5}$$

where L is the length of the channel, d is the diameter, ρ is the density and ω the velocity of the fluid. The frictional coefficient ξ for incompressible laminar flow is given by the Hagen-Poiseuille law as a function of the Reynolds number (Re):

$$\xi = \frac{64}{Re}, \tag{4.6}$$

and for turbulent flow in smooth tubes the Blasius expression can be used:

$$\xi = \frac{0.3164}{Re^{0.25}}, \tag{4.7}$$

which is valid for Reynolds numbers between 3000 and 10^5.

1 GASPAK, Cryodata Inc., Version 3.3 (1999).
2 This model was implemented by S. Grohmann.

The pressure drop in two-phase flow inside a heated tube arises from flow friction and from fluid dynamics effects, which are due to the increased momentum of the heated fluid. In homogeneous two-phase flow (vapour and liquid phases are well mixed), the frictional pressure gradient component can be calculated using the Chisholm equation [25]:

$$\left(-\frac{dp}{dz}\right)_{\mathrm{F}} = \left(-\frac{dp}{dz}\right)_{\mathrm{l}} + \mathrm{C}\cdot\left[\left(-\frac{dp}{dz}\right)_{\mathrm{l}}\left(-\frac{dp}{dz}\right)_{\mathrm{g}}\right]^{\frac{1}{2}} + \left(-\frac{dp}{dz}\right)_{\mathrm{g}}, \tag{4.8}$$

which relates the two-phase flow frictional pressure gradient (subindex F) to that of the liquid (subindex l) and gas (subindex g) fractions flowing alone. The Chisholm parameter C depends on the Reynolds numbers of the liquid and gas flow and is tabulated in literature. The single-phase pressure gradients can be calculated using Equation 4.5.

The two-phase momentum pressure drop arises from the acceleration of the fluid when the vapour fraction increases in the heated sections of the cooling pipe. By denoting the gas fraction at the inlet and outlet of the heated pipe x_1 and x_2, the accelerational pressure gradient can be expressed as [40]:

$$\Delta p = \frac{\Phi_{\mathrm{M}}(\dot{m}_{\mathrm{g}} + \dot{m}_{\mathrm{l}})^2}{A^2 \rho_{\mathrm{l}} g}, \tag{4.9}$$

where $\dot{m}_{\mathrm{l}}$ and $\dot{m}_{\mathrm{g}}$ are the liquid and vapour mass flow, A is the cross-sectional area of the pipe, ρ_{l} is the liquid density, g is the acceleration due to gravity and Φ_{M} the momentum pressure drop parameter:

$$\Phi_{\mathrm{M}} = \left[\frac{(1-x_2)^2}{\alpha_{\mathrm{l},2}} - \frac{(1-x_1)^2}{\alpha_{\mathrm{l},1}}\right] + \left(\frac{x_2^{\,2}}{\alpha_{\mathrm{g},2}} - \frac{x_1^{\,2}}{\alpha_{\mathrm{g},1}}\right)\frac{\rho_{\mathrm{l}}}{\rho_{\mathrm{g}}}, \tag{4.10}$$

where α stands for the volume fraction.

Pressure drop measurement

The pressure drop at our test section is the sum of the pressure drop at the pre-heater (Δp_{PH}) and at the module (Δp_{M}) pipes:

$$\Delta p = \Delta p_{\mathrm{PH}} + \Delta p_{\mathrm{M}}. \tag{4.11}$$

The pressure drop is clearly dominated by the Δp at the smaller diameter pipe, as can be inferred from Equation 4.5. The inner diameter and roughness of the module CuNi pipe was measured at the Metrology service at CERN, since they are both important parameters for the model. The inner diameter of the module capillary is 524 ± 3 μm. For the pre-heater stainless steel pipe, the inner diameter is considered to be the nominal 250 ± 7 μm.

The pressure drop was measured for three different mass flow rates, namely 50 mg/s, 60 mg/s and 70 mg/s, as a function of the quality factor (the power applied to the pre-heater varied from 0 W to 8 W and no heat load was applied at the module). The pressure drop is:

$$\Delta p = p_{\mathrm{TI}} - p_{\mathrm{outlet}}, \tag{4.12}$$

where p_{TI} is the pressure given by the sensor located at the thermal interface, and p_{outlet} is the pressure corresponding to the saturation temperature TS8.

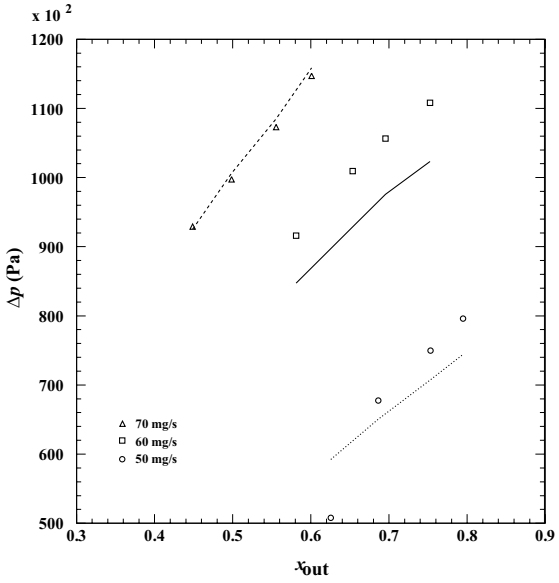

Figure 4.4 Comparison between experimental data (points) and homogeneous two-phase flow pressure drop model (lines) for mass flows of 50 mg/s, 60 mg/s and 70 mg/s. x_{out} is the quality factor at the module outlet.

As shown in Figure 4.4, where experimental and theoretical data are compared, the model is in good agreement with the measured data for high mass flow rates. Systematic deviations for lower mass flow rates are observed. The largest differences in the pressure drop are found for a mass flow rate of 60 mg/s. However, this maximal difference of 80 mbar yields a difference in temperature less than 0.5 K, which is perfectly tolerable for the purpose of our measurement. The homogeneous pressure drop model was therefore used for the correction of the saturation temperature when the data was analysed.

4.4 Results on the thermal behavior of the module

ΔT as a function of the heat load

Three tests were carried out at different mass flow rates to study the dependence of the temperature distribution through the module (ΔTs[1]) with the heat load (electronics and thermal radiation). The conditions at which these tests were performed are summarized in Table 4.3.

Two-phase argon with a vapour fraction of 0.2 entered the module section (Equation 4.1), and was partially evaporated at the module, the outlet vapour fraction (x_{out}) changing from 0.2 to 0.85 depending on the power applied to the APV-25 and radiation heater, on the mass flow rate, and the heat transfer coefficient (Equation 4.2).

1 Temperature difference with respect to the bulk temperature of argon.

Table 4.3 Operating conditions of thermal tests 1,2 and 3.

	Test 1	**Test 2**	**Test 3**
mass flow	30 mg/s	120 mg/s	30 mg/s
P_{PH}	1.9 W	9.4 W	1.9 W
x_{in}	0.2	0.2	0.2
P_{APV}	0 - 2.5 W	0 - 4.5 W	0 - 2.5 W
P_{RAD}	0 W	0 W	300 mW
x_{out}	0.2 - 0.85	0.2 - 0.5	0.2 - 0.85

A thermal shield was cooled down to minimize thermal radiation. For tests 1 and 2, no power was applied to the thermal radiation heater located at the back part of the support plate. 300 mW were applied in the case of test 3, so as to simulate the thermal radiation that the module would receive from a vacuum chamber at 300 K (i.e. the Roman Pot, see Chapter 2).

The results of test 1 are displayed graphically in Figure 4.5. A linear dependence of the temperature with the heat load is observed. This indicates that the heat transfer coefficient is not strongly depending on the applied heat load, or the variation is negligible compared to the thermal resistance on the glue layers of the module. The heat transfer coefficients have been calculated for each measuring point using the experimental correlations from [27] (see Section 4.5) and range from 5000 W/m^{2}K to 10000 W/m^{2}K.

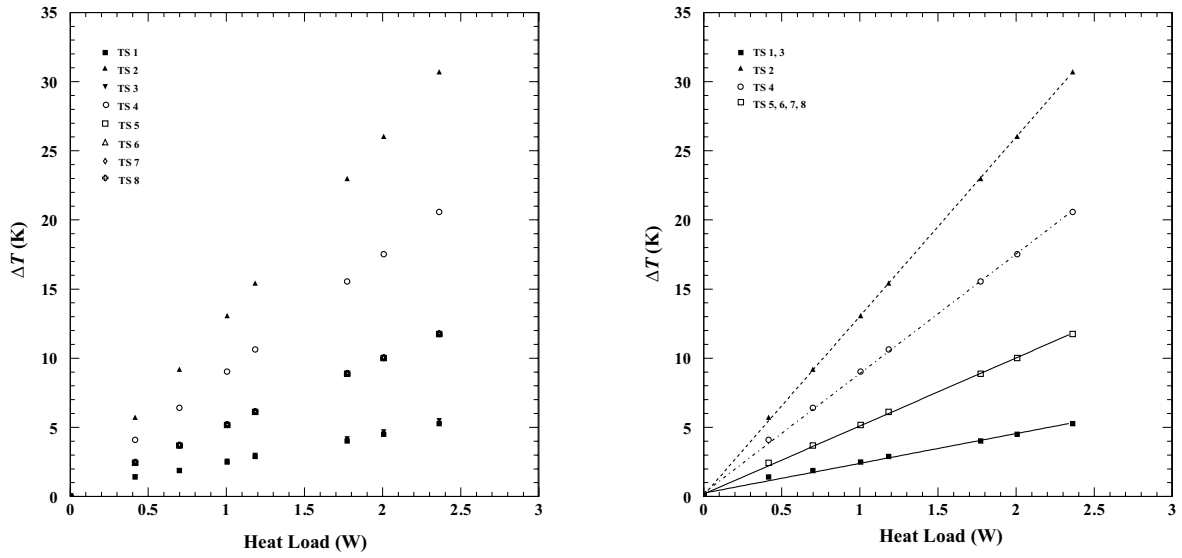

Figure 4.5 Dependence of ΔT with applied heat load on the electronics. Experimental data (left) and data linear fits (right).

The linearity is lost close to zero heat load. This is due to parasitic heat loads that come from poor thermal anchoring of the thermometer leads. Therefore, the low heat load points are affected by a larger error. This was taken into account when fitting the data. The linear fit parameters for each temperature sensor for test 1, are listed in Table 4.4.

Table 4.4 Parameters from the linear fit for each temperature sensor (test 1).

Sensor	***a* (K)**	***b* (K/W)**	**σ_a (K)**	**σ_b (K/W)**
TS1	0.241	2.155	$0.72\ 10^{-1}$	$0.49\ 10^{-1}$
TS2	0.084	12.957	$0.72\ 10^{-1}$	$0.49\ 10^{-1}$
TS3	0.203	2.254	$0.72\ 10^{-1}$	$0.49\ 10^{-1}$
TS4	0.246	8.648	$0.71\ 10^{-1}$	$0.49\ 10^{-1}$
TS5	0.171	4.928	$0.72\ 10^{-1}$	$0.49\ 10^{-1}$
TS6	0.198	4.946	$0.72\ 10^{-1}$	$0.49\ 10^{-1}$
TS7	0.202	4.947	$0.72\ 10^{-1}$	$0.49\ 10^{-1}$
TS8	0.192	4.924	$0.72\ 10^{-1}$	$0.49\ 10^{-1}$

Four different groups of thermometers can be clearly distinguished. As expected, the hotests points are located on the APV25 chips, where the heat load is actually applied. For a heat load of 1.77 W, equivalent to 6 APV25, a ΔT of 23.2 K is measured at this location. Due to the low thermal conductivity of the alumina, the hybrid remains rather hot, with a ΔT of 15.7 K for this heat load. The points located on the silicon support plate and sensor (TS5 to TS8), far away from the cooling pipe, are at similar temperatures. This points out the extremely good thermal conductivity of silicon at low temperature, and the convenience of using it as a constructive material for cryogenic modules with a flat temperature distribution along the structure. Less than 10 K difference between the bulk temperature of the coolant and the silicon sensor is found when the heat load is 1.77 W. The smallest temperature differences (ΔT = 5 K) are found on the silicon pitch adapter (TS1 and TS3) located on top of the cooling pipe.

The results for tests 2 (higher mass flow) and 3 (with thermal radiation heat load) are show in Figure 4.6. As can be seen in the figures, the points have been fitted to a line. The slope and intercept parameters for the three tests are compared in Table 4.5.

From the fitted parameters, it can be concluded that there are no major differences between the three runs: there is not a strong dependence of the temperatures with the mass flow rate, and thermal radiation induces only marginal differences on the temperatures along the module.

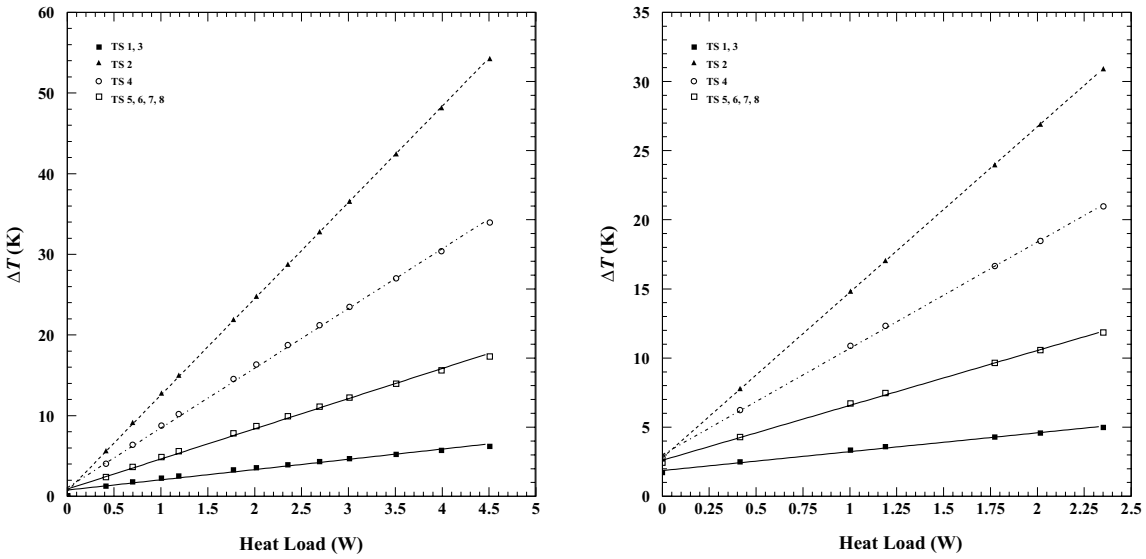

Figure 4.6 Results for thermal tests 2 (left) and 3 (right).

Table 4.5 Fit parameters comparison between tests 1, 2 and 3.

	a_1	b_1	a_2	b_2	a_3	b_3
TS1, TS3	0.241	2.155	0.771	1.273	1.865	1.363
TS2	0.084	12.957	0.632	11.934	2.784	11.972
TS4	0.246	8.648	1.058	7.410	3.007	7.691
TS5 to TS8	0.171	4.928	0.889	3.741	2.605	3.971

ΔT as a function of the inlet vapor fraction

In order to study the thermal behaviour of several modules working in series, the dependence of the ΔTs with the inlet quality factor was studied. The operating conditions of this test (test 4) are summarized in Table 4.6.

The temperature at the module is nearly constant with the quality factor. This shows again that the variation of the heat transfer coefficient with the quality factor is negligible compared to the glue layer thermal resistance at the module and that working with the modules in series is very convenient. As shown by Figure 4.7 the maximum variation of the ΔT with the quality factor is of 2.5 K for the set of thermometers located on the silicon support plate and sensor (TS 5, 6, 7 and 8).

Table 4.6 Operating conditions of test 4.

	Test 4
mass flow	60 mg/s
P_{PH}	3 - 7 W
x_{in}	0.1 - 0.6
P_{APV}	1.77 W
P_{RAD}	0 W
x_{out}	0.1 - 0.85

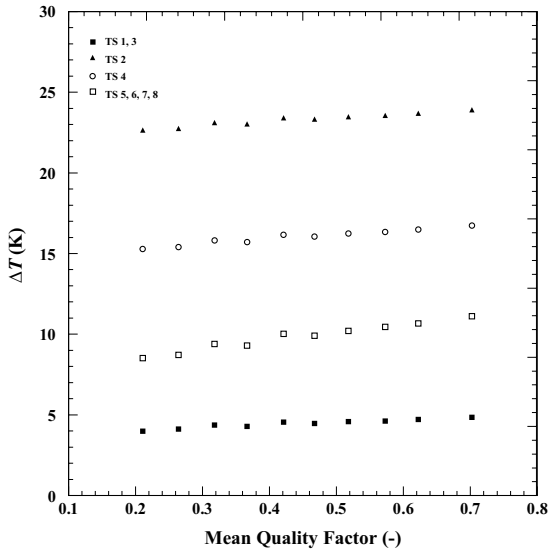

Figure 4.7 Dependence of the ΔT with the module inlet vapour fraction (test 4).

Instabilities under certain inlet conditions

The hydraulic design is particularly important in two-phase microtube cooling systems, as unsteady flow in parallel microchannels has been observed by a number of authors [41][42]. The instabilities are caused by obstruction of individual flow channels with growing vapour bubbles, and the resulting pressure waves can then cause flow reversal through a low impedance by-pass, such as a parallel channel. Such instabilities will not appear in microtube heat exchangers with a single flow path. Therefore, modules should run in series and not in parallel.

Certain operating conditions close to the saturation state at the module inlet may lead to instabilities. Two runs (30 mg/s and 75 mg/s mass flow rates) were dedicated to observe these instabilities, by entering the module with slightly sub-cooled liquid and by changing the heat load applied on the module. When the heat load is too small to ensure stable nucleation the system begins to oscillate between sub-cooled liquid, liquid superheating and evaporation.

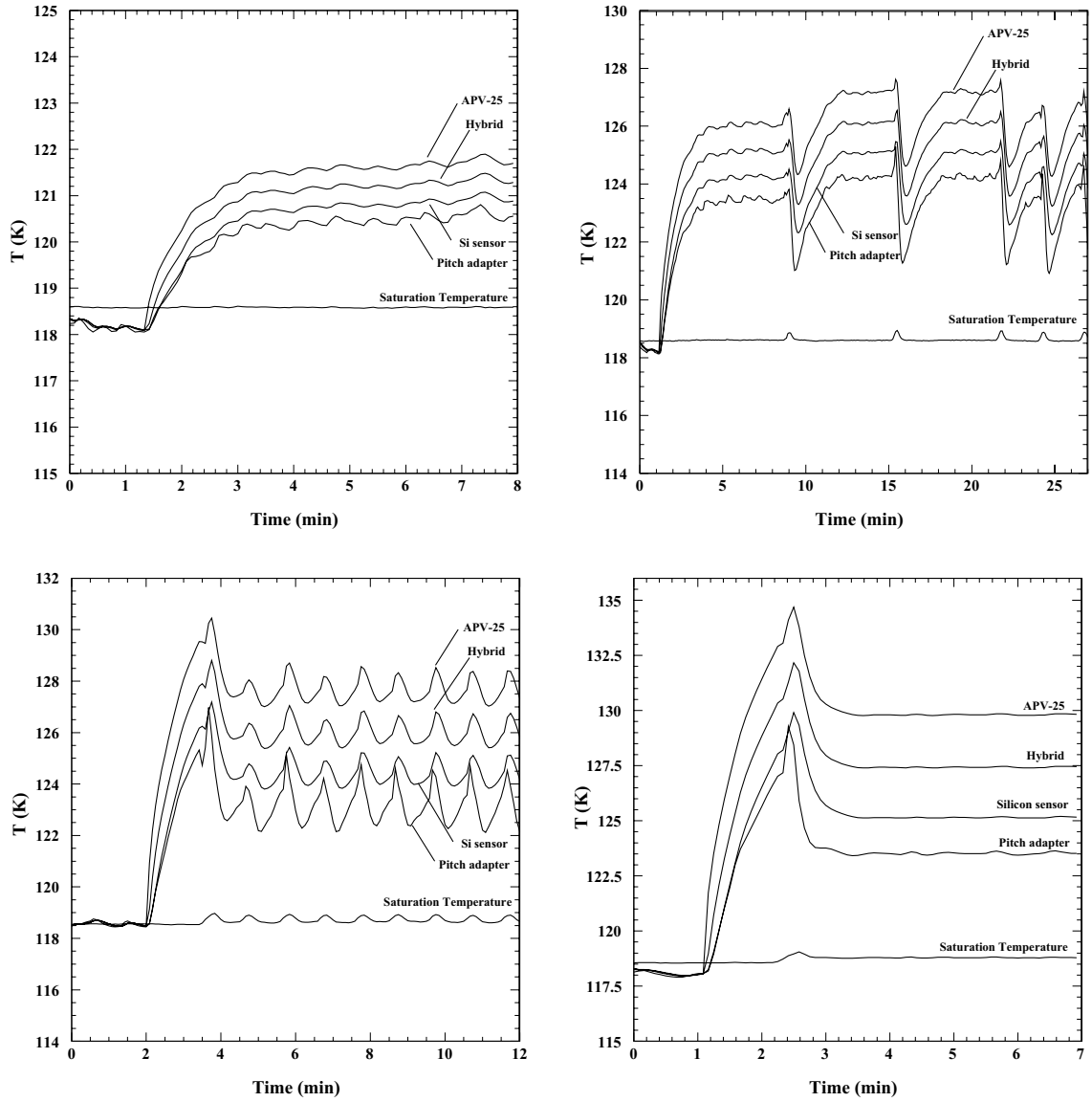

Figure 4.8 Instabilities observed when entering the module with sub-cooled liquid. Low mass flow rate (30 mg/s). From left to right and top to bottom: P_{APV} = 0.11 W, 0.27 W, 0.42 W and 0.59 W.

Figure 4.8 shows the results for the low mass flow rate tests. The power applied to the pre-heater was of 1.47 W in order to provide a few degrees sub-cooled liquid at the module inlet. The first figure on the left shows the temperature evolution with time at four different locations when we apply 0.11 W at the module APVs. The oscillations indicate that we are working either with superheated or sub-cooled liquid, and the two-phase flow regime is not established. When the heat load on the module is increased (second plot, P_{APV} = 0.27 W), enough heat flux to start boiling is reached. The heat transfer coefficient increases and therefore the temperature difference decreases dramatically, gaining again a state where there is not enough heat flux density to initiate boiling. The heat transfer coefficient decreases, and consequently the temperatures rise again. The boiling appears associated with an increase of the saturation temperature (increase on the circuit pressure). The period of these oscillations becomes

shorter when the heat load at the module increases (third figure, P_{APV} = 0.41 W), and seems to reach the two-phase flow regime when the heat load is around 0.59 W (last figure).

Similar behaviour is observed for a high mass flow (75 mg/s). In this case the pre-heater was set to 3.73 W and about 0.5 W is needed at the module to establish a stable two-phase flow regime.

Stability of the compressor system

With a proper design, microtube cooling systems can be operated in the nucleate boiling dominated regime at very high stability. Figure 4.9 shows the thermal response of the cold modules during 1 hour, when the nominal heat load for 6 APVs (P_{APV} = 1.78 W) is applied to the module. Inlet quality factor is x_{in} = 0.3 (P_{PH} = 4.7 W) and the mass flow $\dot{m}$ = 52 mg/s. The temperature deviations are of the order of a few tenths of mK, and the mass flow presents deviations of less than 1 mg/s.

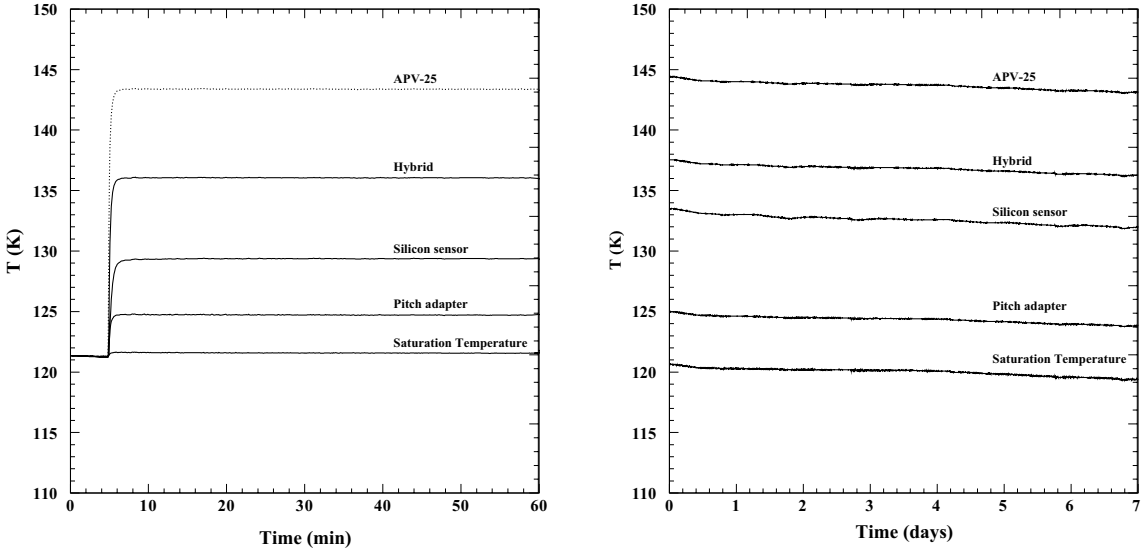

Figure 4.9 Left: 1 hour stability test. Data are recorded with a time interval of 5 seconds. Right: 1 week stability test. Data recorded with a time interval of 1 minute.

A longer test over a period of 1 week was also conducted (Figure 4.9). The operating conditions are the following: inlet quality factor x_{in} = 0.27, P_{APV} = 1.78 W and $\dot{m}$ = 92 mg/s. The system is run without any active control, except for the compensation heater for the cryocooler installed at the thermal interface. The results show that there is no oscillation or instability. The maximum temperature shift of 1.5 K (TS5) over the full week is due to a loss of system pressure, which is caused by a small leak in the warm part of the circuit, and loss of power at the pre-heater. The mass flow changes by 10 mg/s.

4.5 Comparison with thermal simulations

A new finite element model

A new ANSYS model was prepared to simulate the exact operating conditions of the module thermal tests. A particular effort was done to describe the carbon fiber composite (CFC) spacer geometry and

reproduce the heat load distribution applied at the ceramic heaters of the tested module (see Figure 4.10). The mesh was refined at the spacer, where the largest temperature gradients are expected close to the cooling pipe. Both hexahedral and tetrahedral elements where used in this model. The spatial resolution on this region is 500 μm in the *x* and *y* axis and less than 100 μm along the *z* axis, as can be seen in the detail of Figure 4.10. The resolution on the rest of the module is of 1 mm in the *y* axis and higher than that in the two other coordinates. The new model has about 90000 nodes and 80000 elements.

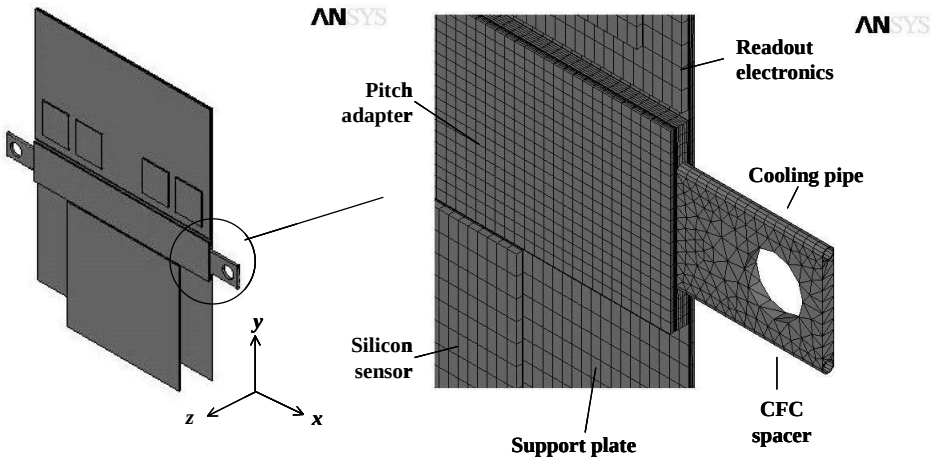

Figure 4.10 The new model reproduces the geometry of the carbon fiber composite spacer (CFC), where the mesh is refined.

Heat transfer coefficient of two-phase argon

The module thermal tests were carried out with two-phase flow argon circulating along the 500 μm inner diameter pipe. The onset nucleate boiling heat flux (Equation 2.11) determines if the flow regime is in convective boiling or nucleate boiling. The heat transfer coefficient is given by Equation 2.12 and Equation 2.13, respectively.

In the latter case, both the nucleate boiling (α_{nb}) and the convective boiling (α_c) components contribute to the total heat transfer coefficient α in the following way:

$$\alpha = \sqrt[3]{\alpha_c^3 + \alpha_{nb}^3}\,. \tag{4.13}$$

The heat transfer coefficients used for the simulation of thermal test 1 are presented in Table 4.7. The operating flow regime was nucleate boiling ($\dot{q} > \dot{q}_{onb}$). The values shown in the table account for the total heat transfer coefficient α (Equation 4.13).

Since the convective boiling component is strongly depending on the quality factor, the heat exchanger section was divided in five sections, and the heat transfer coefficients have been calculated assuming a linear dependence of the quality factor with the pipe length.

Table 4.7 Heat transfer coefficients used in the simulation of the thermal test 1.

Thermal Test 1	**Point 1**	**Point 2**	**Point 3**	**Point 4**	**Point 5**	**Point 6**	**Point 7**
Heat Load APV (W)	0.42	0.69	1.00	1.18	1.77	2.00	2.36
x_{in}	0.20	0.20	0.20	0.20	0.20	0.20	0.20
x_{out}	0.32	0.38	0.47	0.54	0.68	0.75	0.84
HTC 1 (W/m^{2}K)	4195	5380	6440	6996	8596	9160	9956
HTC 2 (W/m^{2}K)	4219	5404	6465	7023	8622	9186	9982
HTC 3 (W/m^{2}K)	4244	5429	6492	7052	8651	9216	10012
HTC 4 (W/m^{2}K)	4269	5455	6521	7083	8681	9247	10042
HTC 5 (W/m^{2}K)	4295	5482	6550	7115	8711	9274	10055

Effective glue layer

The finite element model takes into consideration the effective glue layer between the silicon support plate and the ceramic readout electronics. It is possible to evaluate with reasonable accuracy the effective glued area between these pieces because the dot pattern can be seen through the alumina. This area was only slightly more than 20 % of the total area.

The glue layer was therefore far from being continuous, which would be the most convenient from a thermal and mechanical point of view. In fact, this is the reason why the measured temperatures at the hybrid and APVs during the thermal tests were showing much higher values than in the very first simulations of the modules, presented in Chapter 2, which assume continuous glue layers. This points out the importance of a good gluing pattern and set of glue dispenser parameters.

Comparison between simulation and measurements

The temperature distribution predicted by the finite element model is shown by Figure 4.11, where a heat load of 2 W on the APV25s is simulated. The results of the simulations are summarized in Figure 4.12, where the ΔTs are plotted as a function of the heat load applied at the readout electronics. The simulation also distinguishes four groups of thermometers and shows a linear dependence of the temperature with the heat load. The linear fit parameters for each temperature sensor for the simulated data of test 1 are listed in Table 4.8.

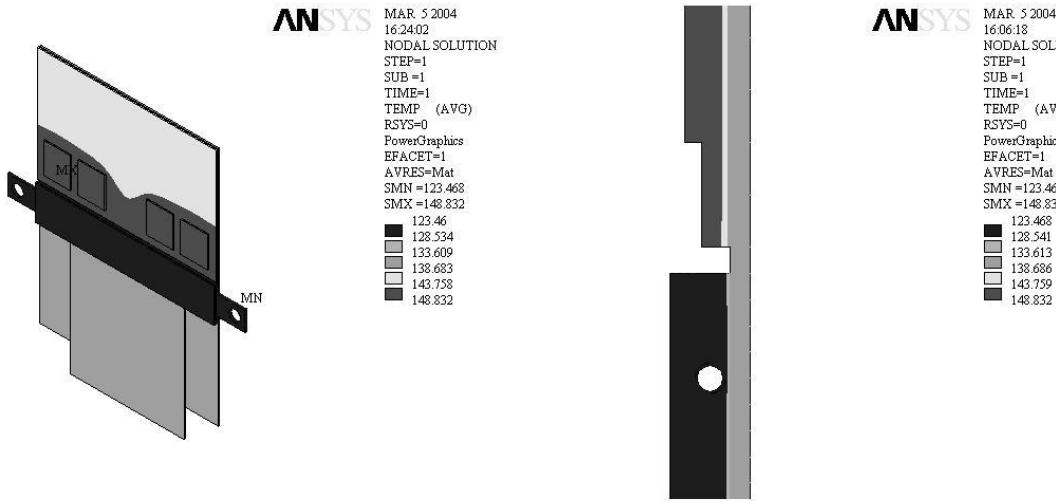

Figure 4.11 The temperature distribution of the prototype module with a heat load of 2 W at the readout electronics, and an inlet and outlet vapour fraction of 0.2 and 0.75 respectively.

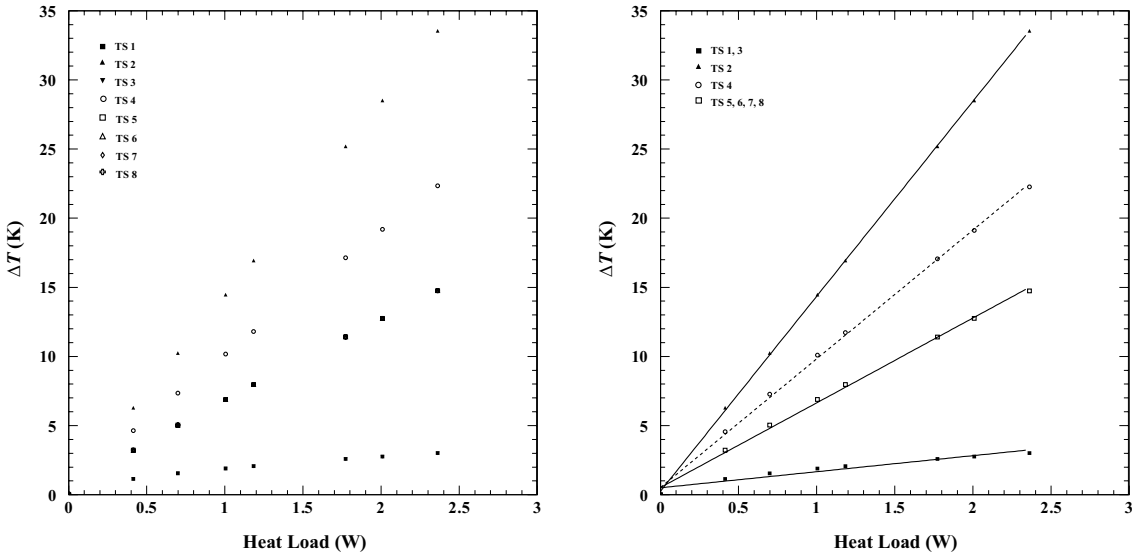

Figure 4.12 Simulated temperature on the module as a function of the heat load applied on the electronics.

The experimental and simulated curves are compared in Figure 4.13. There are systematic differences between experimental and simulation temperatures, which increase with the heat load. The temperatures predicted by the simulation for the pitch adapter (TS1 and TS3) are colder than the experimental results. The maximum temperature difference in this case is of 2.8 K. The differences become smaller and of opposite sign for the warmer points on the sensor, support plate and readout electronics. The maximum temperature differences on the APV25 is only of 1.1 K.

Table 4.8 Parameters from the linear fit of simulated data for each temperature sensor (test 1).

Sensor	*a* (K)	*b* (K/W)	σ_a (K)	σ_b (K/W)
TS1	0.504	1.162	$0.65\ 10^{-1}$	$0.46\ 10^{-1}$
TS2	0.259	14.102	$0.65\ 10^{-1}$	$0.46\ 10^{-1}$
TS3	0.504	1.153	$0.65\ 10^{-1}$	$0.46\ 10^{-1}$
TS4	0.523	9.310	$0.65\ 10^{-1}$	$0.46\ 10^{-1}$
TS5	0.523	6.123	$0.65\ 10^{-1}$	$0.46\ 10^{-1}$
TS6	0.521	6.133	$0.65\ 10^{-1}$	$0.46\ 10^{-1}$
TS7	0.521	6.133	$0.65\ 10^{-1}$	$0.46\ 10^{-1}$
TS8	0.522	6.133	$0.65\ 10^{-1}$	$0.46\ 10^{-1}$

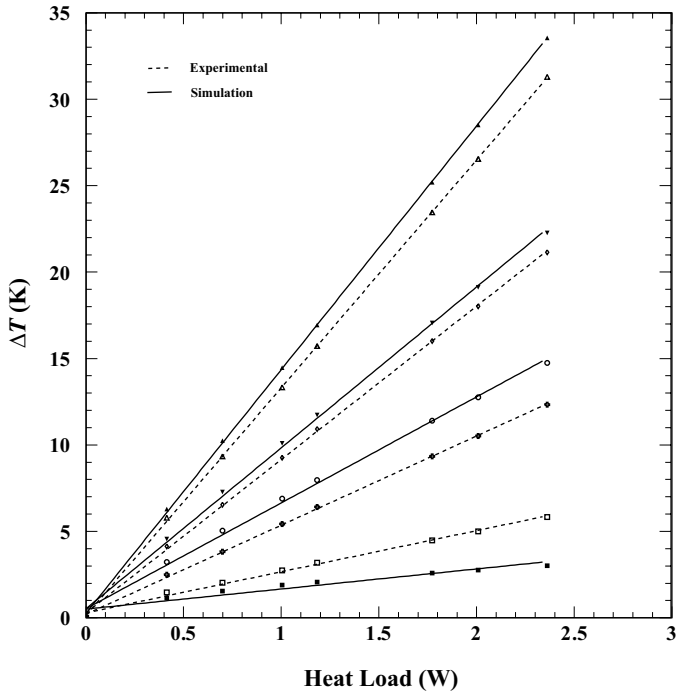

Figure 4.13 Comparison between experimental and simulated data for test 1.

The fact that the simulated pitch adapter temperature is lower than in the tests, points out the fact that the carbon fiber composite spacer (CFC), where the largest gradients are expected, can only be modeled to a certain extent. A large number of assumptions needed to be made to model the spacer, such as a constant thermal conductivity of the CFC (not as a function of temperature). Besides, the glue layer which surrounds the CuNi pipe cannot be reproduced accurately. Despite all the assumptions that need to be made, the temperature distribution along the module can be described with a reasonable accuracy.

4.6 Discussion on the results

The cooling prototype system used during these tests has proven to work in a reliable way. An automatization of this setup and further effort to make a compact design, could make of it a candidate to be used either in beam and irradiation tests or at experiments, in the tunnel close to the interaction point.

Working with sub-cooled liquid at the module inlet can lead to instabilities in the flow regime, and therefore substantial changes in the heat transfer coefficient and temperature distribution through the module. It is therefore strongly recommended to work with well developed two-phase flow (inlet vapour fraction of 0.2 seems very good). The design of a cooling system where the modules are connected in series proves to be convenient and stable.

Silicon is an excellent heat spreader. The use of silicon as a constructive material leads to flat temperature profiles in the sensor and the module structure, and has the advantage of not inducing extra thermal stress when cooling down.

The maximum temperature difference between the module and the bulk temperature of the fluid is of the order of 25 K for a heat load on the module equivalent to 6 APV25. This result can be improved, as first simulations had shown (Chapter 2), if continuous and thin glue layers can be achieved. Automatization of the gluing is therefore desired once found the glue dispenser parameters (pressure and needle diameter) and glue pattern that can ensure a continuous layer of less than 100 μm.

The thermal resistance due to the glue layers dominates the thermal behaviour, other factors as the heat transfer coefficient dependence on flow parameters, being less relevant. Thermal radiation leads to marginal increases on the temperature.

The finite element model has been adjusted with the thermal tests. It was enough to include an effective glued area factor on the glue layer under the hybrid to obtain simulated results close the experimental ones, with differences of the order of 1 K. The simulations can therefore be used as a tool to predict the temperature distribution of the module, but the results should be taken with a certain criticism, understanding the geometry differences between model and real module, specially when it comes to the glue layers, which is a key parameter in the module thermoelastic design.

Last but not least, the thermal tests have proven that a module built in silicon (sensor, pitch adapter and support plate), alumina (readout electronics) and carbon fiber composite (spacer) with thin Araldite® 2011 glue layers can withstand a large number (> 30) of thermal cycles.